

Modeling Study of Variable Upwelling Circulation in the East China Sea: Response to a Coastal Promontory

ZHIQIANG LIU AND JIANPING GAN

Department of Mathematics and Division of Environment, Hong Kong University of Science and Technology, Hong Kong, China

(Manuscript received 6 August 2013, in final form 4 November 2013)

ABSTRACT

A three-dimensional, high-resolution numerical model is used to investigate processes and dynamics of an intensified upwelling that is induced by a coastal promontory over the East China Sea (ECS) shelf. The center of the intensified upwelling around the promontory has been constantly observed, but, so far, it has been dynamically unexplained. Forced by an idealized southeasterly wind stress, the model results well capture the observed upwelling at the lee of the coastal promontory. The intensified upwelling is formed by a strengthened shoreward transport downstream of the promontory as the upwelling jet veers shoreward. The jet is mainly controlled by a cross-shore geostrophic balance and is largely modulated by both centrifugal acceleration associated with nonlinear advection and by bottom stress. The strengthened shoreward transport is mainly attributed to the cross-shore geostrophic current that is induced by a countercurrent (negative) pressure gradient force (PGF) and partly attributed to the bottom Ekman transport. Based on the analyses of the momentum balance and depth-integrated vorticity dynamics, the authors provide a new explanation for the origin of negative PGF. It is found that the countercurrent PGF is generated by negative bottom stress curl and strengthened by negative vorticity advection downstream of the promontory. While the negative bottom stress curl arises from bottom shear vorticity, the source of negative advection downstream of the promontory is the negative shear vorticity on the seaside of the shoreward-bent jet. Nevertheless, cyclonic curvature vorticity at the bottom and positive vorticity advection in the water column at the promontory weakens the negative PGF. Although nonlinear advection strengthens vorticity advection, it weakens bottom stress curl and has little net effect on the countercurrent PGF.

1. Introduction

We conducted a modeling study of the wind-driven coastal upwelling circulation off the Zhejiang coast (areas boarded by the coastline and the dashed line in Fig. 1a) over the broad East China Sea (ECS) shelf. The ECS coastline runs north–south and is adjacent to the Changjiang estuary (CJE) and Hangzhou Bay (HZB; Fig. 1b). There is a prominent coastal headland at the east tip of the Zhoushan Islands ($\sim 30^\circ\text{N}$, $\sim 122.4^\circ\text{E}$, hereafter referred to as the coastal promontory) and south of HZB. Farther offshore, the isobaths direct southwest–northeastward, parallel to the coast in the southern ECS, but diverge seaward from CJE, toward

the Subei shoal, in the northern part of the ECS shelf, where they form a broad submarine delta < 50 m deep.

Forced by the intense summer East Asian monsoon, strong upwelling centers have been frequently reported during June, July, and August in the ECS. The distinct cold surface waters that are associated with the upwelling centers have notable spatial variation and characterize the summer conditions in the region (Chen et al. 2004).

The strong upwelling at the coastal promontory (Fig. 2) is considered to be one of these centers (Zhao 1993) and was found to be established by the southeasterly monsoon wind stress (Liu and Su 1991). This particular upwelling center was also found to be associated with an intensified cross-shore transport in the frictional bottom boundary layer of the northeastward-flowing Taiwan Warm Current (Yuan et al. 1986). Upwelling around the Zhoushan Islands may also be enhanced by the buoyant plume from the CJE (Zhu 2003). Most recently, Lü et al. (2007, 2006) attributed the upwelling off the Zhejiang

Corresponding author address: J. Gan, Department of Mathematics and Division of Environment, Hong Kong University of Science and Technology, Clear Water Bay, Kowloon, Hong Kong, China.
E-mail: magan@ust.hk

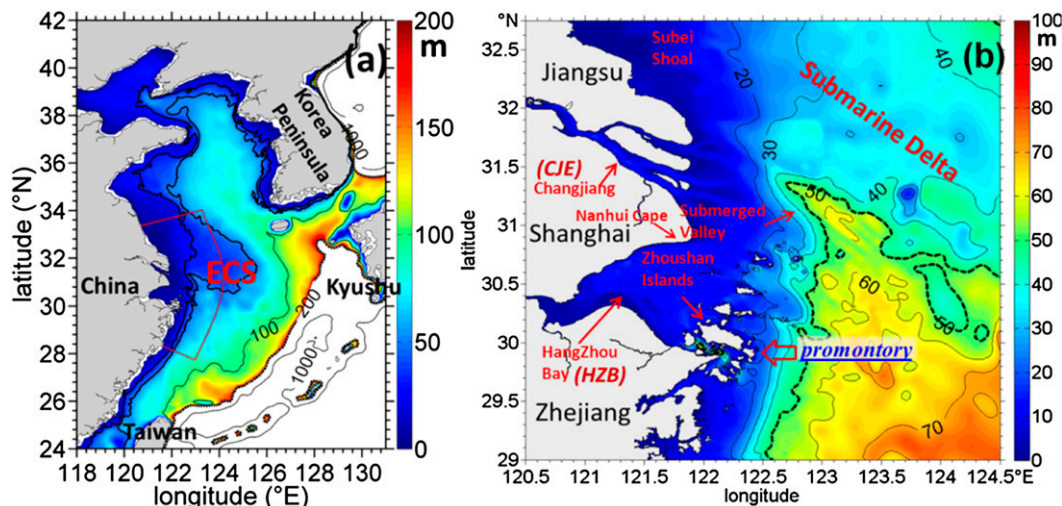


FIG. 1. (a) Bathymetry in the ECS and (b) the zoomed area of the coastal regions around the CJE and HZB. The 50-m isobath is illustrated by the boldface dashed contour. Domain of the numerical model adapted in this study is indicated in (a), and location of the interested promontory is denoted by the thick arrow in (b).

coast to the tidally induced cross-front circulation, as a result of a shoreward pressure gradient force (PGF) that was induced by the baroclinicity of the density front. However, the prominent dynamic effect on the upwelling due to the promontory was not discussed and a complete dynamical rationalization for the prominent upwelling at the unique coastal promontory was not established.

Besides being induced by the alternation of wind in the alongshore direction, alongshore variation of upwelling circulation is often regulated by shelf topography that may involve pronounced alongshore irregularities in the bottom bathymetry (Gan and Allen 2002a; Janowitz and Pietrafesa 1982; Kurapov et al. 2010; Tee 1985). It may also be associated with shelf steepness and width (Allen et al. 1995; Gan et al. 2009; Pringle 2002; Whitney and Allen 2009) and coastline geometry (Arthur 1965; Dale and Barth 2001; Song et al. 2001).

Wind-driven upwelling can be strengthened in the lee of the coastal promontory (Haidvogel et al. 1991), where a pool of cold water in the inshore is often observed (Huyer et al. 2005). The intensified upwelling may be induced by the centrifugally separated coastal jet (Barth et al. 2000). Arthur (1965) showed that the intensified upwelling in the lee of a promontory may be formed by variation in the curvature vorticity due to the meandering of the upwelling jet. It is also generally believed that the strengthened upwelling is mainly linked with the formation of a countercurrent PGF that amplifies the shoreward geostrophic transport (Gan and Allen 2002b; Gan et al. 2009; Song and Chao 2004). The magnitude of this geostrophic cross-isobath transport is often larger than

the bottom frictional transport (Gan et al. 2009). The dynamic interpretation of variable upwelling circulation around the coastal promontory was mainly based on the Euler equation in many previous studies. The frictional effect on the forcing processes, particularly the effect on the dynamic origin of the PGF over the shallower shelf water, has not been discussed. Few studies exist that investigate the responses of wind-driven circulation to variable shelf topography in the ECS.

Following this introduction section, hydrographic measurements are analyzed to elucidate the characteristics of variable upwelling in the ECS (section 2). A three-dimensional circulation model with realistic ECS topography and idealized but representative wind forcing is utilized to simulate the observed upwelling processes (sections 3 and 4), and an idealized conceptual model is then applied to illustrate the dynamics of upwelling circulation around a coastal promontory off the Zhejiang coast (section 5). A summary is provided in section 6.

2. Observations of upwelling

Characteristics of the intensified upwelling in the lee of the coastal promontory in the ECS are shown by the temperature distributions from remotely sensed data and in situ measurements. Spatial distributions of the long-term-averaged (2000–09) wind stress and sea surface temperature (SST) during the summer (June–August) are presented in Figs. 2a and 2b. Horizontal maps of the satellite SST data and the bottom temperature

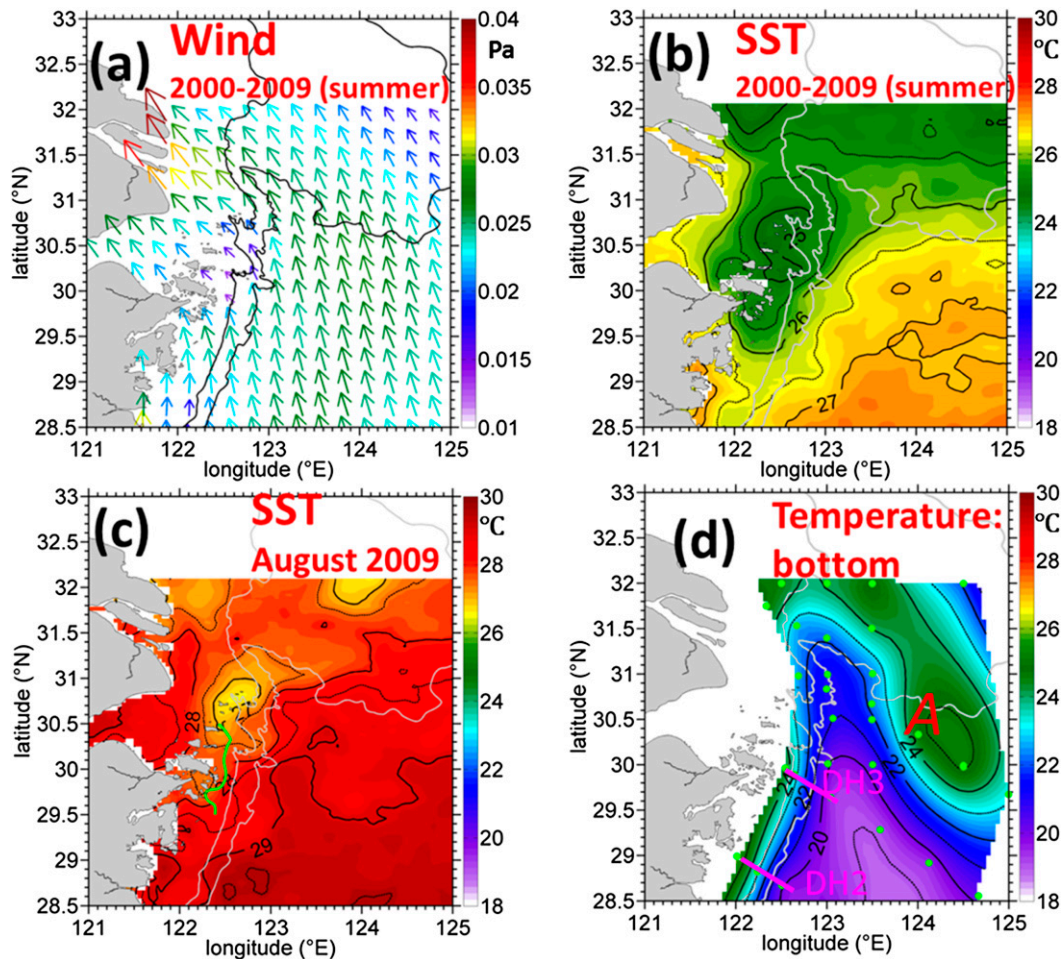


FIG. 2. (a) Long-term-averaged (2000–09) QuikSCAT wind stress vectors (Pa); (b) SST (°C; AVHRR) distributions during the summer (June–August); (c) remotely sensed SST (°C; AVHRR); and (d) bottom temperature (°C) distributions obtained from field measurement conducted from 19 to 31 Aug 2009. The 30- and 50-m isobaths are shown by thick gray contours. The 20-m isobath is presented by the green solid curve in (c), and two sampling cross-shelf transects, DH2 and DH3, during the cruise are illustrated in (d). “A” is a sampling location where its temperature and salinity profiles are used for initialization of the model.

distributions provided by field measurements during August 2009 are shown in Figs. 2c and 2d. The wind stress was obtained from the updated Scatterometer Climatology of Ocean Winds (SCOW) that is derived from long-term Quick Scatterometer (QuikSCAT) data from September 1999 to October 2009 (Risien and Chelton 2008). The remotely sensed SST data were obtained from the Pathfinder, version 5.0, SST dataset from the Advanced Very High Resolution Radiometer (AVHRR) of the National Oceanic and Atmospheric Administration (NOAA).

During summer, upwelling-favorable southerly and southeasterly monsoon winds, with an average wind stress ~ 0.02 Pa, prevailed over the southern and northern parts of the ECS shelf, respectively (Fig. 2a). In response to this upwelling-favorable wind, a belt of relatively cold surface

water formed on the shore side of the 50-m isobath (Figs. 2b,c). It is highlighted by a remarkable cold surface water center to the north of the coastal promontory that is seen in both long term– (Fig. 2b) and cruise time–averaged SST distributions (Fig. 2c). The coastal upwelling current extended this patch of cold water northeastward. The source of the cold surface water at the northern tip of the promontory is associated with the locally strengthened shoreward advance of the cold bottom water (Fig. 2d).

Temperature profiles along the two cross-shelf transects, DH2 and DH3 (Fig. 2d), are shown in Fig. 3. Temperature transect over DH2 indicates that the cold water inside the upwelling belt south of the promontory was formed by the upslope transport of dense shelf water (Fig. 3a). This upwelling was generated by the strong southwesterly wind stress (~ 0.04 Pa) that occurred on

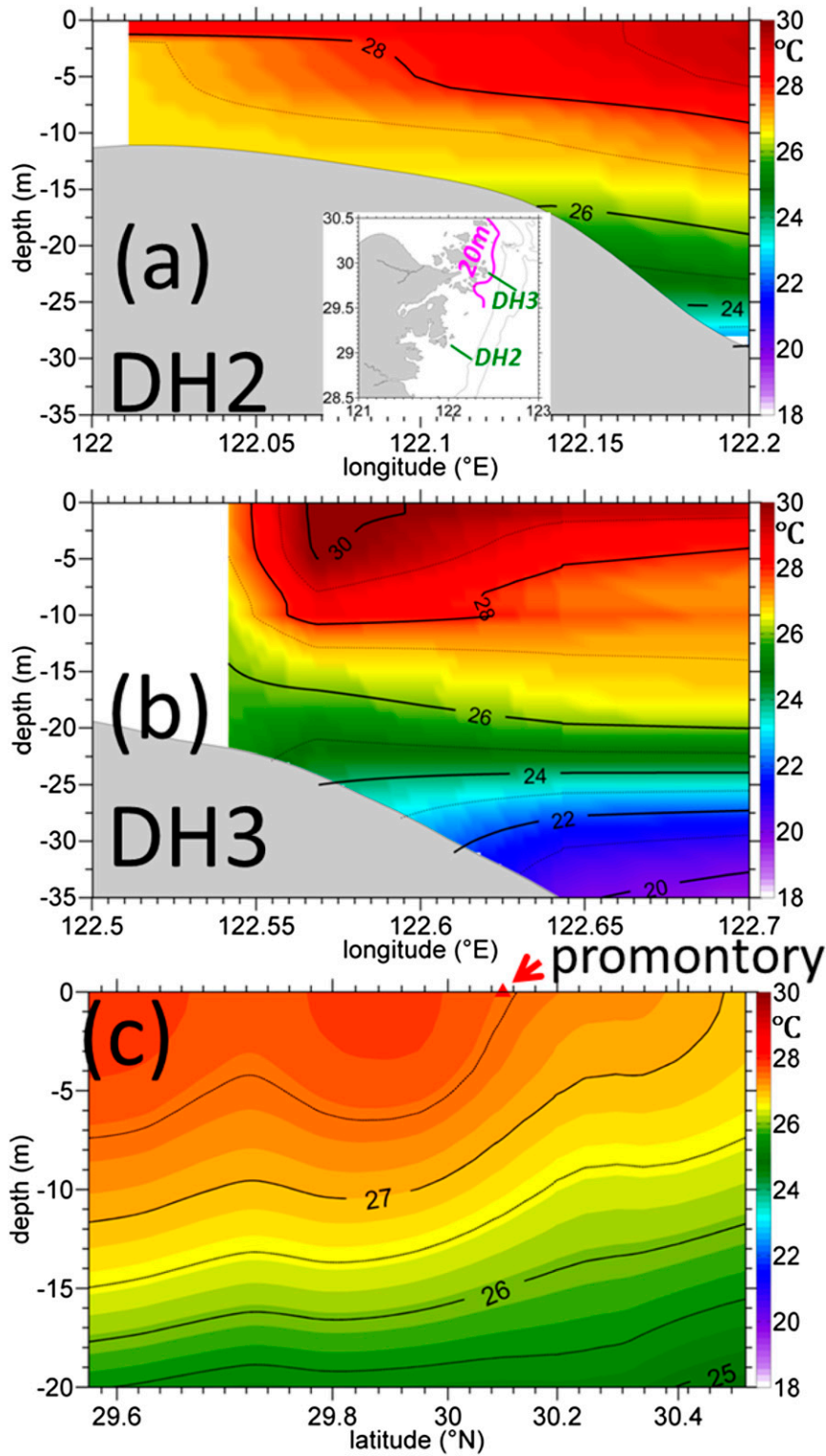


FIG. 3. Observed temperature ($^{\circ}\text{C}$) profiles along the cross-shelf transects of (a) DH2, south of the Zhoushan Islands; (b) DH3, off the Zhoushan Islands; and (c) the transect along the 20-m isobath off the Zhoushan Islands. The sampling was conducted during August 2009. The 20-m isobath and the sampling stations/transects are indicated by the subfigure in (a).

August 19. Much stronger shoreward and upward invasions of cold shelf water are seen off the coastal promontory, along transect DH3 (Fig. 3b), where deep cold water extensively advances shoreward and emerges in the surface layer as represented by the 28°C isotherm. This occurred even when the upwelling-favorable wind weakened during the survey period on August 22. Intensification of the upwelling circulation at the lee of the promontory can also be seen in the temperature profiles along the 20-m isobath off the coast (Fig. 3c). South of the promontory, the water in the upper layer is warmer and more stratified than that in the lee of the promontory where the isotherms tilt extensively upward and deep cold water emerges at the surface. Both in situ and remotely sensed measurements show the existence of intensified upwelling and the associated locally strengthened shoreward and upslope transport in the lee of the coastal promontory. We investigate the process and dynamics related to this intensified upwelling phenomenon using a process-oriented modeling study.

3. Ocean model

The Regional Ocean Modeling System (ROMS) (Shchepetkin and McWilliams 2005), with hydrostatic primitive equations and the Mellor and Yamada (1982) turbulence submodel was applied to the limited coastal area that extends meridionally from 27.75° to 34°N and zonally from 120.7° to 124.2°E (Fig. 4).

A realistic coastline and topography that were digitized from navigation maps published by the Maritime Safety Administration (China) were utilized. The minimum water depth of the model was set as 1 m, and the topography was slightly smoothed to reduce truncation errors. The study area was horizontally discretized and used boundary fitted, orthogonal curvilinear coordinates on a staggered Arakawa C grid (Fig. 4). A higher-resolution horizontal grid (<200m) was used in the CJE and the grid size gradually increased to ~1.5 km in the open ocean. The model was vertically discretized into 30 levels on stretched terrain-following s coordinates (Song and Haidvogel 1994), which formed a vertical grid size less than 1 m in the coastal water. Higher vertical resolution was applied in the surface and bottom boundary layers by substituting the control parameter of s coordinate $\theta_s = 2.5$ at the surface and $\theta_b = 0.8$ at the bottom, respectively.

To better isolate the dynamics for the intensified upwelling, it was to our advantage to force the model with a southeasterly wind stress with a meridional component equal to 0.0181 Pa and a zonal component equal to -0.0125 Pa over the entire model domain. This wind stress was representative of the upwelling-favorable monsoon in summer over the ECS (Fig. 2). Temperature and salinity

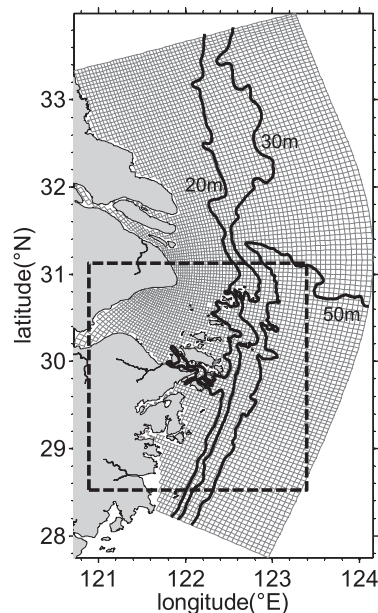


FIG. 4. Curvilinear grid of the coastal ECS model. The coastal region off Zhejiang and the Zhoushan Islands are illustrated by the dashed box. The 20-, 30-, and 50-m isobaths are shown by the black bold lines.

profiles obtained from the field cruise at station A (Fig. 2d) were used to initialize the model. The initial values of the velocities and surface elevation were set to zero. For simplicity, the model was forced by the wind stress for 30 days. The atmospheric heat flux, buoyancy from the Changjiang River, and the effect of the ambient currents were excluded. This assumption was appropriate because we were focusing on the flow response to the coastal promontory.

The model domain includes three open boundaries, and open boundary conditions (OBCs) favorable to the wind-forced shelf circulation (Gan and Allen 2005; Gan et al. 2005; Pringle and Dever 2009) were utilized along the southern and northern boundaries. The OBCs separate the model variables at the open boundary into the forced local part and unforced global part. The variables for the local part, surface elevation η , barotropic velocities \bar{u} and \bar{v} , baroclinic velocities u and v , temperature T , and salinity S at the open boundaries, were obtained from an across-shore, two-dimensional submodel with reduced physics. The variables in the global part were provided by an oblique horizontal radiation condition (Marchesiello et al. 2001). The horizontal momentum advection terms in the model were solved by a third-order, upwind-biased scheme, and the advection terms of the active tracers were calculated by a multidimensional positive definite advection algorithm (MPDATA). Horizontal diffusion processes

were represented by a harmonic viscosity with constant eddy coefficients ($5 \text{ m}^2 \text{ s}^{-1}$).

4. Characteristic response of upwelling

The wind-forced upwelling general circulation over the ECS shelf is shown by surface elevation and surface and bottom velocity vectors on days 5 and 30 (Fig. 5). In response to the upwelling-favorable southeasterly wind stress, the cross-shore gradient of surface elevation increases from day 5 to day 30 and develops a northeastward alongshore current at the surface. The alongshore current first appears in the waters shoreward of the 30-m isobath on day 5 and then evolves into a prominent jet with its core situated over the relatively steep shelf in the strip bounded by the 30- and 50-m isobaths on day 30. This coastal jet is prevented from being attached to the coast due to well-mixed shallow water <10 m deep. As a result of the bottom frictional effect of the upwelling alongshore currents, shoreward currents occur in the bottom layer. Similar to the alongshore currents, the region with strong shoreward currents at the bottom shifts seaward on day 5 to the same strip between the 30- and 50-m isobaths on day 30.

The coastal upwelling circulation is highly variable in the alongshore direction, particularly in the region with complex coastline topography around the Zhoushan Islands. The isolines of η veer shoreward (cyclonically) in the lee of the coastal promontory around the islands. Concurrently, the currents intensify and form maximum shoreward currents at the bottom around the promontory. The intensity of this unique coastal circulation around the Zhoushan Islands is strengthened and expanded seaward from day 5 to day 30 when currents reach quasi steady state.

The surface and bottom temperature distributions on days 5 and 30 are well correlated with the evolution of cross-shore transport in response to the southeasterly winds (Fig. 6). At the surface, warmer water on day 5 is replaced by relatively cold water on day 30 with the stronger cooling occurring in the lee of the promontory. This cold surface water apparently originated from the upwelling of the shoreward-advected bottom offshore water. The cold water at the bottom advanced shoreward to the coastal region from the offshore region of the 30-m isobath from day 5 to day 30, following the development of the upwelling circulation (Figs. 5b,e).

The much stronger shoreward-advected bottom water at the lee of the coastal promontory forms a minimum temperature at the surface and is carried farther downstream by the alongshore current. Similar but relatively weak cold surface centers also exist in the lees of different coastal promontories around 29.5° and 28.5°N , suggesting the robust upwelling enhancement by the

coastal promontory. Because of the advection of the alongshore current, a distinct northeastward cold surface water belt appears over the inner shelf shoreward of the 30-m isobath.

Intensification of upwelling in the lee of the coastal promontory is also shown by the time-averaged velocity (i.e., u and v) and temperature profiles along a meridional transect (Fig. 7) located off the promontory (Fig. 6d). The data were averaged over time on day 30. The northward coastal jet (v) intensifies toward the Zhoushan Islands at about 29.96°N , reaches a maximum speed at the promontory, and weakens farther north. Seaward ($u > 0$) and shoreward ($u < 0$) transport occurs in the surface and bottom layers upstream of the promontory, respectively, where the waters are stratified. Intensified shoreward transport ($u < 0$) enhances first at the bottom, then through the entire water column in the lee of the coastal promontory with a maximum shoreward u ($< -0.1 \text{ m s}^{-1}$) at $\sim 10 \text{ km}$ from the promontory. The shoreward-advected colder deep water upwells at the northern tip of the promontory to form the pool of cold surface water that is seen in the observations (Figs. 2b,c).

5. Dynamics at the coastal promontory

Because of the extreme complexity of the bathymetry surrounding the entrance of HZB, a simulation with idealized topography focusing on the promontory (Fig. 8) is adapted to better illustrate dynamic processes around the promontory. This idealized topography preserves the spatial scale and topographic characteristics of the real promontory around the Zhoushan Islands. The model domain here extends 250 (800) km in the zonal (meridional) directions, and the water depth was set to be 30 m inside the HZB (Fig. 8a). The waters over the shelf linearly deepen in the offshore direction x with the sloping parameter $dh/dx = 1.0 \times 10^{-4}$, where h is the water depth. The shelf topography is uniform in the alongshore direction y with $dh/dy = 0$, and a periodic OBC was applied to the southern and northern open boundaries. Other implementations and forcing were set the same as before. To isolate and identify the effect of the coastal promontory on the variable upwelling circulation, we used horizontally and vertically homogeneous density. As presented in the following sections, the general characteristics of upwelling response around the promontory obtained from this idealized model are well consistent with those in the realistic model presented in the previous sections.

a. Alongshore variation of flow

We present the results of the quasi steady state on day 20 (Fig. 8). The isolines of the surface elevation convex

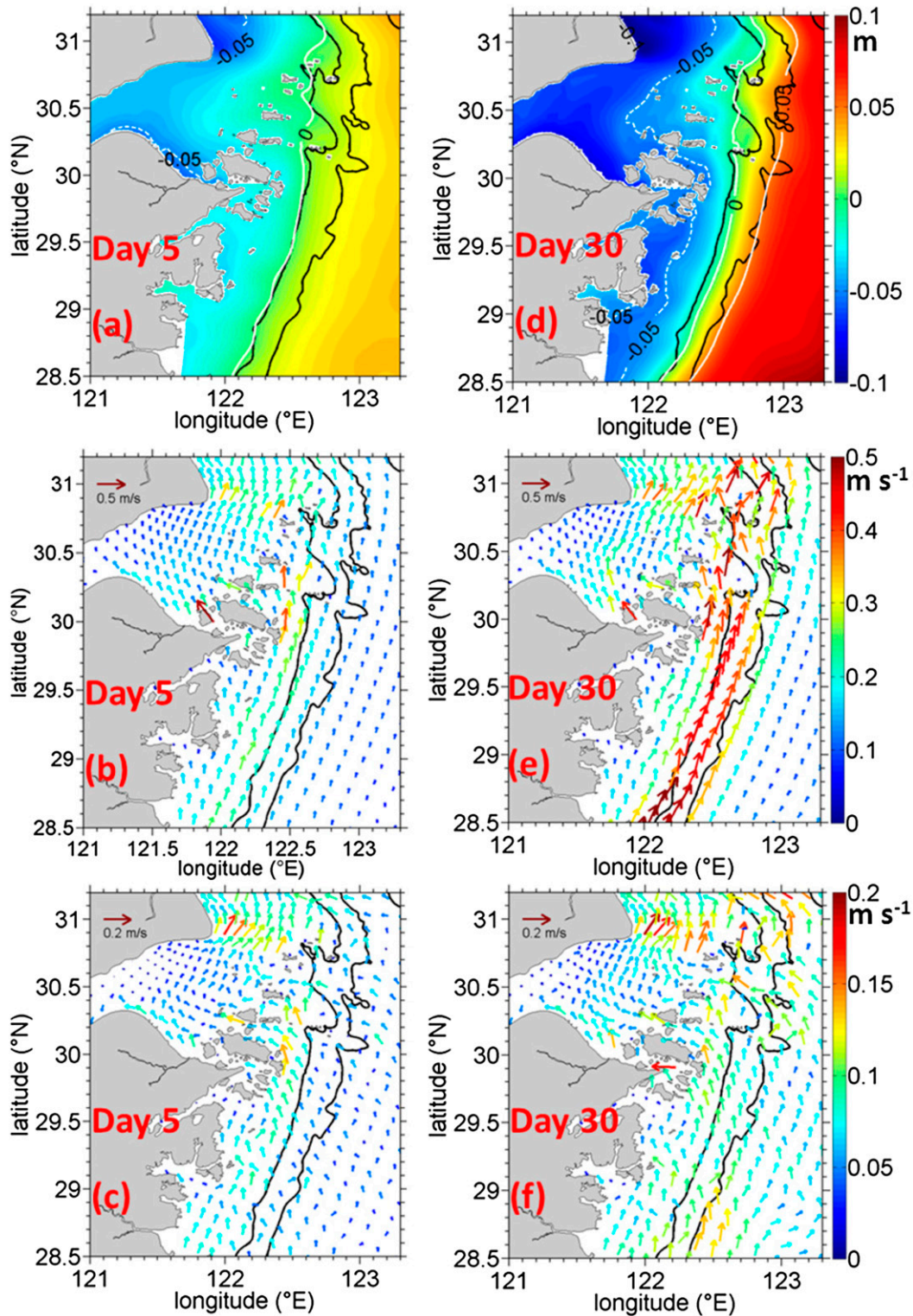


FIG. 5. Daily average of (a),(d) surface elevation (m); (b),(e) surface velocity (m s^{-1}); as well as (c),(f) bottom velocity vectors (m s^{-1}) on (left) day 5 and on (right) day 30, respectively. The 30- and 50-m isobaths are illustrated by the black boldface lines.

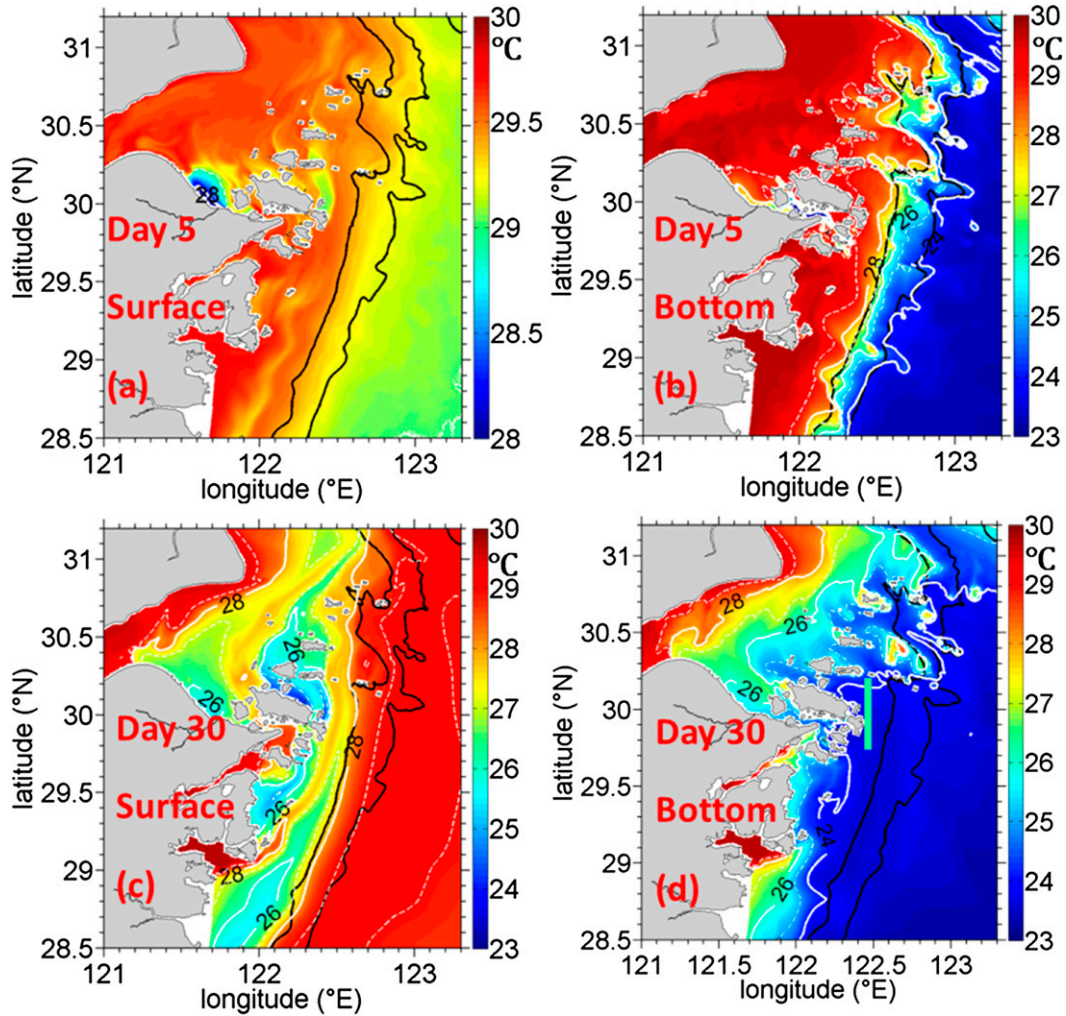


FIG. 6. (a),(c) Surface and (b),(d) bottom temperature ($^{\circ}\text{C}$) distributions averaged on (top) day 5 and (bottom) day 30, respectively. The 30- and 5- m isobaths are shown by the black boldface lines. A meridional transect that crosses the waters off the Zhoushan Islands is indicated by the green line in (d). To better highlight evolution of the upwelling circulation, the scale of the color bar in (a) is shorter than the others.

shoreward at the entrance of HZB and form a northward surface elevation gradient that is qualitatively similar to the results captured in the simulation with realistic topography. A northward coastal jet at the surface accelerates as it approaches the coastal promontory and rotates cyclonically (Fig. 8b). Farther downstream, the upwelling jet weakens and bends anticyclonically to flow northeastward. In the bottom layer (Fig. 8c), shoreward currents exist over the entire domain. The strongest shoreward currents, however, occur in the lee of the promontory and lead to an intensified upwelling of shelf water at the northern tip of the Zhoushan Islands (Fig. 6).

Alongshore variation of upwelling circulation can also be shown by the three-dimensional velocity (i.e., u and v) in the alongshore transect at $x = 85$ km on day 20 in

Fig. 9. The northward upwelling jet (i.e., v) extends over the entire water column with decreasing magnitudes from the surface to the bottom. Similar to the model results with realistic topography (Fig. 7), the coastal current (i.e., v) intensifies toward the promontory ($y = 290$ km) and reaches a maximum speed with $v > 0.2 \text{ m s}^{-1}$ before it weakens downstream of the promontory. Shoreward ($u < 0$) and seaward ($u > 0$) currents exist in the bottom and surface layers upstream of the promontory, respectively. Downstream, a shoreward velocity (i.e., u) occurs in the entire water column (Fig. 9b). The maximum shoreward velocities of $u < -0.1 \text{ m s}^{-1}$ exist ~ 10 km downstream of the promontory. This strong onshore transport advects deep cold water shoreward to form the distinct upwelling zone as in Fig. 6.

Variations in the surface elevation, depth-averaged relative vorticity ξ , and depth-averaged velocity (i.e., \bar{u} and \bar{v}) along the transect at $x = 85$ km (Fig. 10) are used to further illustrate the alongshore variations induced by the promontory. Surface elevation increases downstream of the promontory (Fig. 10a), as a result of its shoreward veering, and generates a southward alongshore PGF along the transect. The depth-averaged vorticity is very small upstream of the promontory, but becomes positive in the lee of the promontory where the flow veers cyclonically. It shifts anticyclonically about 20 km farther downstream. Both the alongshore (i.e., \bar{v}) and shoreward (i.e., \bar{u}) currents strengthen toward the promontory (Fig. 10b), but the \bar{v} reaches

a maximum at the promontory, while maximum \bar{u} exists ~ 10 km downstream of the promontory. The embedded dynamics that determine these alongshore variations of the upwelling currents around the promontory is presented next.

b. Momentum and vorticity balances

We first use term balances in both the depth-averaged momentum and depth-averaged vorticity equations to show the dynamic characteristics that may control the processes of the intensified upwelling in the lee of the coastal promontory. The depth-averaged momentum equation in Cartesian coordinates and with no stratification is written as

$$\begin{cases} \text{ACCEL}_x \\ \frac{\partial \bar{u}}{\partial t} \end{cases} = \underbrace{f\bar{v}}_{\text{COR}_x} - \underbrace{[(\bar{u}, \bar{v}) \cdot \nabla] \bar{u}}_{\text{HADV}_x} - \underbrace{g\eta_x}_{\text{PGF}_x} + \underbrace{\frac{\tau_{sx}}{\rho_0 D}}_{\text{SSTR}_x} - \underbrace{\frac{\tau_{bx}}{\rho_0 D}}_{\text{BSTR}_x} + \underbrace{K_h \nabla^2 \bar{u}}_{\text{HVISC}_x}$$

$$\begin{cases} \text{ACCEL}_y \\ \frac{\partial \bar{v}}{\partial t} \end{cases} = \underbrace{-f\bar{u}}_{\text{COR}_y} - \underbrace{[(\bar{u}, \bar{v}) \cdot \nabla] \bar{v}}_{\text{HADV}_y} - \underbrace{g\eta_y}_{\text{PGF}_y} + \underbrace{\frac{\tau_{sy}}{\rho_0 D}}_{\text{SSTR}_y} - \underbrace{\frac{\tau_{by}}{\rho_0 D}}_{\text{BSTR}_y} + \underbrace{K_h \nabla^2 \bar{v}}_{\text{HVISC}_y},$$
(1)

where subscripts x and y denote the momentums in cross- and alongshore directions, respectively. The symbol ∇ is the Hamiltonian operator, and variables τ_s and τ_b are the surface and bottom stresses. The reference density and coefficient of horizontal viscosity are represented by ρ_0 and K_h , respectively. The terms in Eq. (1) are acceleration (ACCEL), Coriolis force (COR), horizontal nonlinear advection (HADV), PGF, wind stress (SSTR), frictional bottom stress (BSTR), and the horizontal viscous term (HVISC). The ageostrophic pressure gradient force (AGE = PGF + COR) is adopted to consider the combined effects of COR and PGF.

Taking the curl of the vertically averaged momentum Eq. (1) and substituting the continuity equation [$\nabla \cdot (\bar{u}, \bar{v}) = 0$], we get the depth-averaged vorticity equation in the f plane:

$$\begin{aligned} \underbrace{\nabla \times \text{ACCEL}}_{\frac{\partial \xi}{\partial t}} &= \underbrace{\nabla \times \text{HADV}}_{-[(\bar{u}, \bar{v}) \cdot \nabla] \xi} + \underbrace{\nabla \times \text{COR}}_{(f \cdot \nabla)(\bar{u}, \bar{v})} \\ &\quad - \underbrace{\nabla \times \left(\frac{\tau_b}{\rho_0 D} \right)}_{\nabla \times \text{BSTR}} + \underbrace{\nabla \times \text{HVISC}}_{K_h \nabla^2 \xi}, \end{aligned} \quad (2)$$

where ξ is the vertically averaged relative vorticity. The terms in Eq. (2) are the tendency of the ξ ($\nabla \times \text{ACCEL}$), advection of ξ ($\nabla \times \text{HADV}$), stretching of the vortex tube ($\nabla \times \text{COR}$), bottom stress curl ($\nabla \times \text{BSTR}$), and lateral

frictional effect ($\nabla \times \text{HVISC}$). The wind stress curl is zero in this study and vorticity tendency term is small and negligible.

1) ALONG-ISOBATH BALANCES

The balances of momentum terms in Eqs. (1) and (2) along the transect at $x = 85$ km were averaged on day 20 and are presented in Fig. 11. The northward-flowing coastal current, which is dominated by the geostrophic balance in the cross-shelf direction (Fig. 11a), is amplified near the promontory by an increase in the cross-shelf pressure gradient PGF_x . This is the result of the centrifugal acceleration (HADV_x) of the cyclonic rotation of the coastal current and bottom stress (BSTR_x). The balance is defined by

$$\text{PGF}_x = \text{COR}_x + \text{HADV}_x + \text{BSTR}_x. \quad (3)$$

The negative AGE_x around the promontory indicates a net negative (shoreward) PGF_x that may contribute to the shoreward motion of the currents.

The balance in the alongshore momentum equation (Fig. 11b) is highlighted with the existence of the intensified shoreward transport in the lee of the promontory, as represented by positive COR_y , which is chiefly balanced by a distinct southward PGF_y . From a careful comparison of the momentum balance in the alongshore direction with that in the cross-shore direction, one finds

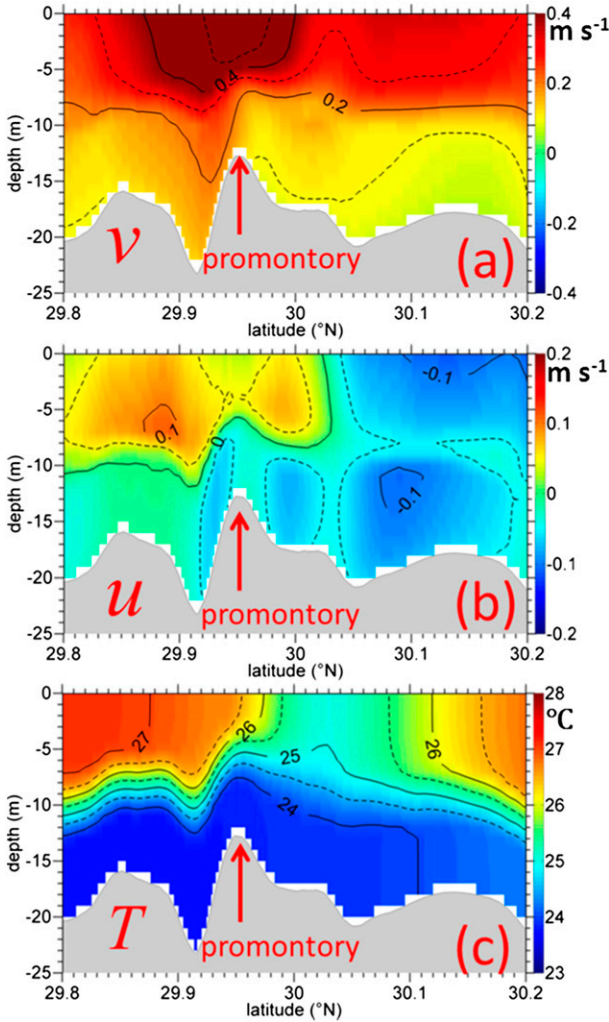


FIG. 7. (a) Along- (m s^{-1}) and (b) cross-shore (m s^{-1}) velocities, and (c) temperature ($^{\circ}\text{C}$) distributions along the meridional transect off the Zhejiang coast (green line in Fig. 6d). The model results are averaged on day 30. Positive values in v and u represent the northward and eastward velocities in the along- and cross-shore directions, respectively.

that the maximum alongshore velocity occurs at the promontory ($y = 290 \text{ km}$), while the maximum shoreward transport exists 10 km farther downstream ($y = 300 \text{ km}$). Because the bottom frictional transport in the alongshore momentum balance is much smaller, it is conceivable that PGF_y is the main cause for the intensified shoreward transport. We, however, have little knowledge about the origin of PGF_y in the momentum balance.

We may further search for the cause of PGF_y by examining the vorticity balance in Eq. (2) (Fig. 11c). Positive bottom stress curl ($\mathbf{V} \times \text{BSTR}$) amplifies around the promontory, mainly balances the negative stretching term ($\mathbf{V} \times \text{COR}$), and partly balances the negative nonlinear advection term ($\mathbf{V} \times \text{HADV}$). Downstream

of the promontory ($y = 290 \text{ km}$), the nonlinear advection term turns positive and enhances the stretching effect. The result shows that the balance between the nonlinear vorticity advection and bottom stress curl leads to a large negative stretching term downstream of the promontory. The coincidence of the stretching term and PGF_y , in fact, suggests that the formation of stretching by nonlinear advection and bottom stress curl terms contributes to the formation of the negative alongshore PGF_y (Mertz and Wright 1992), as we explicitly show next.

2) ORIGIN OF NEGATIVE ALONGSHORE PGF_y

So far, we identified the importance of negative PGF_y on the intensified upwelling in the lee of the coastal promontory. However, the origin of PGF_y could not be explicitly identified from either the depth-averaged momentum or vorticity balances. In fact, the alongshore PGF_y (Fig. 11b) may be linked to the depth-integrated vorticity dynamics as shown by Eq. (4), according to Gan et al. (2013):

$$\begin{aligned} \underbrace{\frac{-1}{\rho_0} P_{y^*}^b}_{\text{PYB}} &= \underbrace{\frac{1}{D_{x^*}} \bar{\mathbf{v}} \times (\tau_b - \tau_s)}_{\text{BSC}} + \underbrace{\frac{1}{D_{x^*}} J(\psi, \xi)}_{\text{RVA}} \\ &+ \underbrace{\left(\frac{\|\bar{\mathbf{v}}\|^2}{2} \right)_{y^*}}_{\text{GMF}} + \underbrace{\frac{1}{D_{x^*}} \bar{\mathbf{v}} \times \int_{-D}^0 K_h \nabla^2 \mathbf{v}}_{\text{CHV}}, \end{aligned} \quad (4)$$

where subscripts x^* and y^* denote partial differentiation in the directions normal to and along the isobaths, respectively. The term $(-1/\rho_0)P_{y^*}^b$ is the along-isobath bottom PGF (Fig. 11b); D_{x^*} is the slope of the shelf (1.0×10^{-4}); J is the Jacobian determinant; ψ is the transport streamfunction; $\psi_y = -\bar{u}D$ and $\psi_x = \bar{v}D$; and \mathbf{v} is the vector form of the depth-averaged velocity (i.e., \bar{u} and \bar{v}). Term BSC of Eq. (4) is net stress curl in the water column, and equals the bottom stress curl when the wind stress curl is absent. The net stress curl in the water column, the relative vorticity advection, the gradient of momentum flux, and the curl of horizontal viscosity in Eq. (4) are denoted as BSC, RVA, GMF, and CHV, respectively. As shown by Gan et al. (2013), $(-1/\rho_0)P_{y^*}^b$, termed as PYB, is equivalent to the depth-averaged along-isobath pressure gradient force PGF_y (Fig. 11b) when stratification is small. In the following sections, PYB is adapted to denote PGF_y .

Terms in Eq. (4), along the transect at $x = 85 \text{ km}$, averaged over day 20, are presented in Fig. 12a. The countercurrent (negative) PYB around the promontory, which is responsible for the locally intensified shoreward

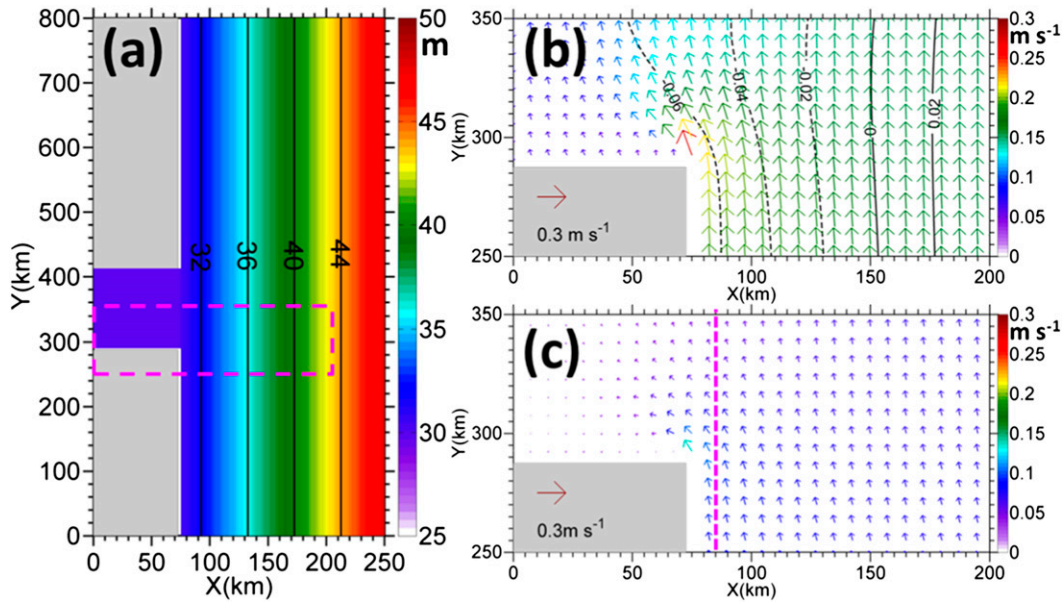


FIG. 8. (a) Domain and bathymetry of the idealized model, and (b) surface velocity (m s^{-1}) and elevation (m) as well as (c) bottom velocity (m s^{-1}) vectors on day 20. (b) and (c) are shown in the region around the promontory as indicated by the pink box in (a). A meridional transect on the shelf off HZB is indicated by the dashed line in (c).

transport and upwelling, is clearly originated from the negative BSC with the contribution by RVA downstream of the promontory. The magnitudes of negative BSC and positive RVA increase gradually from ~ 20 km upstream of the promontory and reach their maxima at the promontory where a large portion ($\sim 39\%$) of negative BSC (about $-4.3 \times 10^{-6} \text{ m s}^{-2}$) is offset by positive RVA ($\sim 1.7 \times 10^{-6} \text{ m s}^{-2}$). Both terms become negative ~ 7 km downstream from the promontory and reinforce PYB. The positive RVA exists around the promontory due to centrifugal acceleration as flow turns cyclonically, and is negative downstream from the promontory due to the negative vorticity advection on the seaside of the shoreward-bent jet.

As a result of the spatial distribution of BSC and RVA, the largest magnitude of negative PYB (about $-5.0 \times 10^{-6} \text{ m s}^{-2}$) occurs 10 km downstream of the promontory ($y = 290$ km). Both GMF and CHV are very small. As shown by the vorticity stretching term in Fig. 11 from Eq. (2) and negative PYB in Fig. 12 from Eq. (4), it is quite clear that both BSC and nonlinear vorticity advection (RVA) contribute to the formation of PYB and thus to the intensified shoreward transport and upwelling in the lee of the coastal promontory.

While the correlation of vorticity advection with the structure of the jet flow around the promontory is obvious, the correlation between the bottom stress curl and jet flow is ambiguous. Under the approximation of the quadratic drag law with the absence of wind stress curl

(Gan et al. 2013), BSC in Eq. (4) can be expressed as (see also the appendix)

$$\overbrace{\frac{1}{D_{x^*}} \nabla \times \frac{\tau_b}{\rho_0}}^{\text{BSC}} = \overbrace{\frac{C_d}{D_{x^*}} \|\mathbf{V}_b\| \xi_{bc}}^{\text{BSC}_c} + \overbrace{\frac{2C_d}{D_{x^*}} \|\mathbf{V}_b\| \xi_{bs}}^{\text{BSC}_s}, \quad (5)$$

where $C_d = 3 \times 10^{-3}$ is the bottom drag coefficient, and (\mathbf{V}_b) is the magnitude of the bottom velocity. The terms BSC_c and BSC_s of Eq. (5) represent the contributions of bottom curvature (ξ_{bc}) and bottom shear (ξ_{bs}) vorticity to the BSC, respectively. Thus, the formation of BSC in Eq. (4) is directly correlated with the bottom vorticity arising from the spatial variation of the flow field around the promontory.

Contributions from both ξ_{bs} and ξ_{bc} to BSC intensify at the lee of the promontory, but have opposing effects (Fig. 12b). The term ξ_{bc} is positive as the result of cyclonic turning of the flow (Fig. 8c) and ξ_{bc} is negative due to velocity shear on the seaside of the shoreward-bent jet. However, the magnitude of BSC induced by curvature vorticity is smaller than that induced by shear vorticity, or $|\text{BSC}_c| < |\text{BSC}_s|$, and the BSC is mainly induced by the formation of bottom shear vorticity (ξ_{bs}) around the promontory, while the bottom curvature vorticity (ξ_{bc}) associated with the cyclonic veering of the flow offsets the BSC_s intensity. In the shelf with relatively uniform topography where ξ_{bc} is small, BSC is mainly determined by

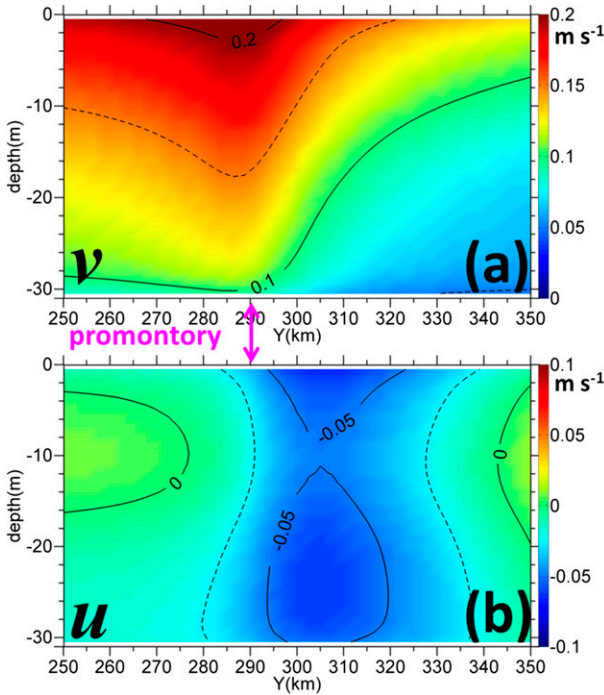


FIG. 9. Vertical transects of (a) along- and (b) cross-shore velocity (m s^{-1}), along the section at $x = 85 \text{ km}$, $250 < y < 350 \text{ km}$ off the entrance of HZB (Fig. 8c) on day 20. Positive values refer to the north- and eastward velocities for v and u , respectively.

shear vorticity, which is often observed on the continental shelf (Gan et al. 2013).

3) BOTTOM STRESS CURL VERSUS NONLINEAR EFFECTS

Unlike the flow over the shelf in Gan et al. (2013), the flow field around the coastal promontory is expected to have much stronger nonlinearity. As shown in Fig. 12a, the joint effect of BSC and RVA forms a negative PYB in the lee of the promontory. The role of RVA on PYB around the promontory ($y = 290 \text{ km}$) is opposite to that downstream of the promontory (Fig. 12a), in which positive and negative values of RVA offset and reinforce PYB, respectively. To show the importance of the nonlinear advection effect, the term balance of Eq. (4) from the model without nonlinear advection is presented in Fig. 13a. We found that the PYB magnitude remains roughly the same as the one in the standard case, in spite of the considerable contribution from RVA being absent.

The main contributor to PYB is from BSC in the linear flow, and our numerical experiment with the absence of bottom stress (without BSTR; Fig. 14) shows that the jet overshoots northward in the promontory without any shoreward intrusion in the water column. Around the

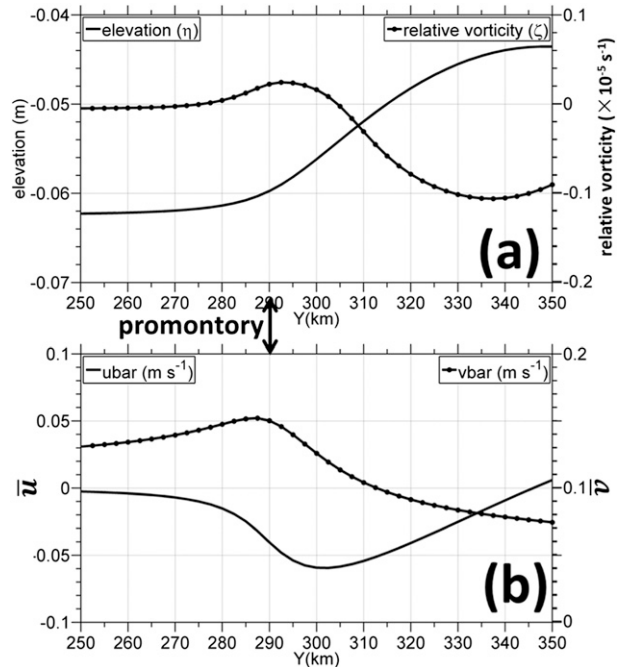


FIG. 10. (a) Surface elevation (m), relative vorticity (s^{-1}) as a function of alongshore distance on day 20; (b) as in (a), but for depth-averaged zonal and meridional velocities (m s^{-1}). In (b), positive values represent east- and northward velocities for zonal and meridional velocities, respectively. All the variables are along the meridional transect at $x = 85 \text{ km}$, $200 < y < 450 \text{ km}$ in Fig. 8c.

promontory, both BSC_c and BSC_s (Fig. 13b) increase as the bottom flows veer cyclonically (also see Fig. 14). Because the inertial term is absent, PYB increases because the increment of BSC_s is larger than the increment of BSC_c . The maximum value of PYB is located slightly closer to the promontory compared to the standard case. Downstream of the promontory, BSC_c decreases dramatically as the flow directs more northward, while BSC_s remains the same as in the standard case. Thus, bottom stress curl or PYB magnitude increases. It should be noted that although BSC_c offsets BSC_s to form PYB, BSC_c or curvature vorticity itself is necessary to shape the flow field for PYB around the promontory.

This and our additional numerical experiments indicate that as the nonlinearity of the flow changes PYB through the vorticity advection, it also largely alters the bottom stress curl through the bottom shear vorticity and curvature vorticity. Their effects, however, offset each other. For example, downstream of the promontory, nonlinearity enhances vorticity advection to reinforce PYB, but it forms a weaker bottom stress curl (Figs. 12a vs 13a). As a result, the effect of nonlinearity of the flow on PYB and upwelling of the promontory is not significant.

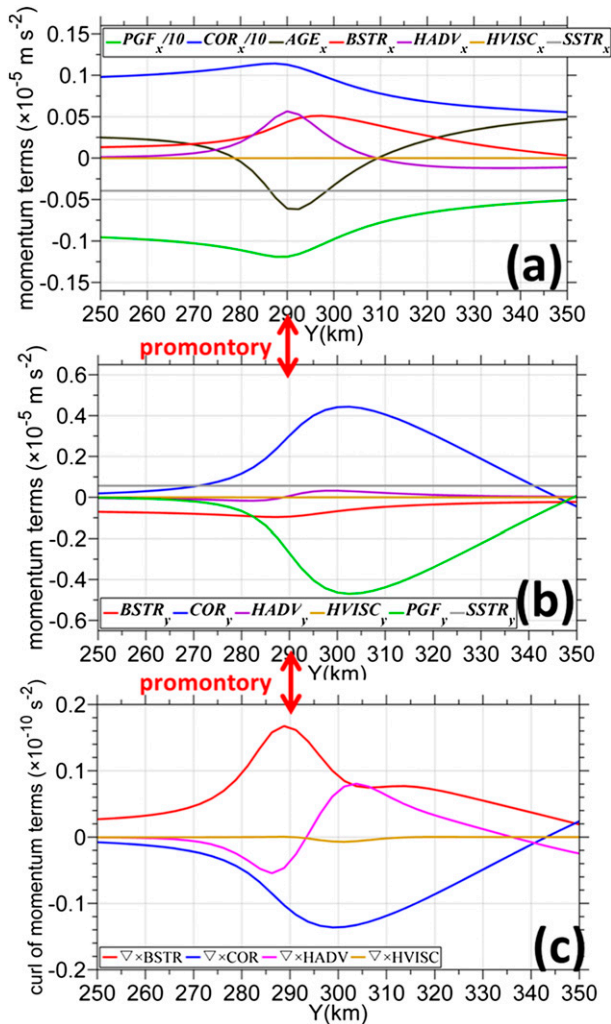


FIG. 11. Terms (m s^{-2}) of depth-averaged momentum equations [Eq. (1)] in (a) cross- and (b) along-shelf directions and (c) terms (s^{-2}) in the depth-averaged relative vorticity Eq. (2) on day 20. Positive values represent the seaward direction in the cross-shelf momentum equation, the northward direction in the along-shelf momentum equation, and the upward direction in vorticity equation, respectively. All the variables are along the meridional transect at $x = 85$ km, $250 < y < 350$ km in Fig. 8c, and PGF_x and COR_x in (a) is divided by 10.

6. Summary and conclusions

Both field measurements and remotely sensed data show the existence of a distinct, intensified upwelling in the lee of the coastal promontory around the Zhoushan Islands in the ECS. The upwelling is a robust phenomenon that is significant to the coastal circulation in the ECS and forms a region of traditional fishery in the Chinese coastal waters. This study conducts a dynamic investigation to understand the underlying process and forcing mechanism of the intensified upwelling that has not been well established.

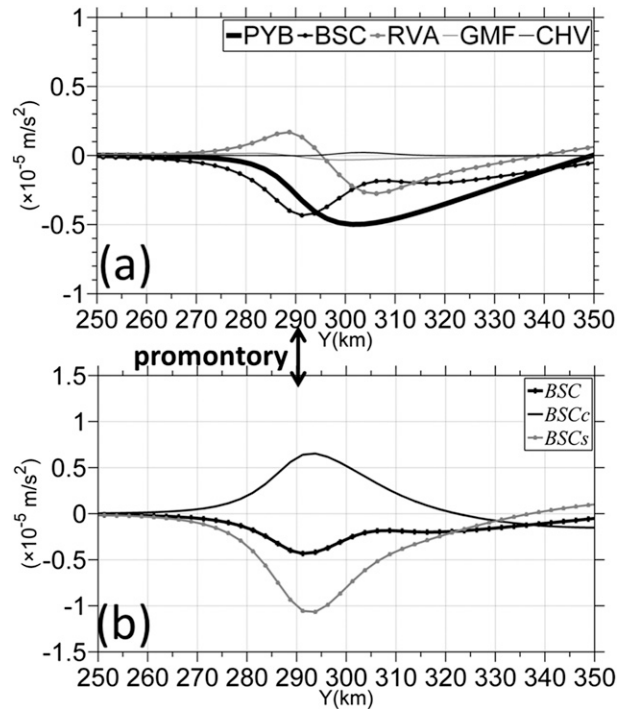


FIG. 12. (a) Terms (m s^{-2}) in the depth-integrated relative vorticity equation [Eq. (4)] on day 20. Positive values represent the northward direction; (b) contributions of bottom shear vorticity (BSC_c) and curvature vorticity (BSC_c) to the total BSC. All the variables are along the meridional transect at $x = 85$ km, $250 < y < 350$ km in Fig. 8c.

A three-dimensional, limited-area numerical model with realistic shelf topography was utilized, and it well captured the observed intensified upwelling processes. This upwelling was found to be induced by the locally strengthened geostrophic shoreward transport as a result of the formation of a countercurrent (negative) PGF around the promontory. A subsequent dynamic analysis based on a similar model but with simplified shelf topography identified the characteristics and origin of the PGF. This study provides a novel explanation of the forcing mechanism for intensified upwelling in the lee of a coastal promontory, and the processes and forcing invoked can be schematically summarized in Fig. 15.

During upwelling, a strong northeastward coastal jet is observed on the shelf between 30- and 50-m isobaths off the Zhejiang coast. A distinct, northeastward, prolonged cold water center is observed on the shore side of the jet, downstream of the promontory, where isolines of surface elevation veer shoreward and the sea level is noticeably lowered around the promontory. The northward upwelling jet is locally accelerated/decelerated in the upstream/downstream of the promontory.

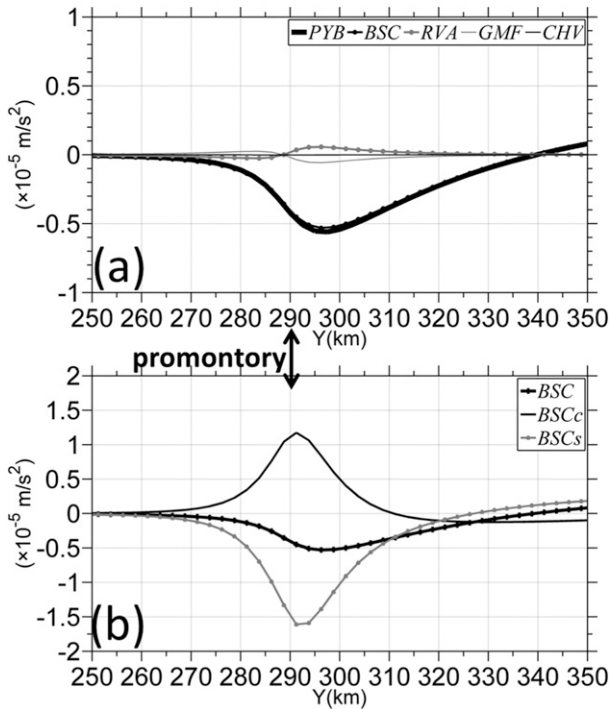


FIG. 13. As in Fig. 12, but for the case without the nonlinear advection term.

It is shown that the jet is generally in geostrophic balance, but is notably modulated by the centrifugal acceleration associated with the cyclonic rotation of the coastal jet and by the bottom stress around the coastal promontory. The importance of the centrifugal effect is also shown by the locally enhanced nonlinear advection of relative vorticity. However, the major vorticity balance in the water column is between the bottom stress curl and stretching of the vortex tube around the promontory, while the nonlinear advection term weakens and strengthens the stretching of the vortex tube around the promontory and downstream of it, respectively. The stretching of the vortex is, in fact, the source of the PGF that forms the intensified shoreward transport and upwelling in the lee of the promontory.

The predominant countercurrent PGF, which generates the extensive onshore transport of shelf water in the lee of the promontory, was explicitly shown to originate from negative bottom stress curl and vorticity advection in the depth-integrated vorticity dynamics. At the promontory, a negative bottom stress curl is offset by a positive vorticity advection induced by cyclonical veering of the jet. This veering, however, set up a negative vorticity advection near the promontory as the seaside of the jet shifts shoreward. Together with the negative bottom stress curl, they reinforce the negative PGF for the intensified upwelling downstream of the promontory.

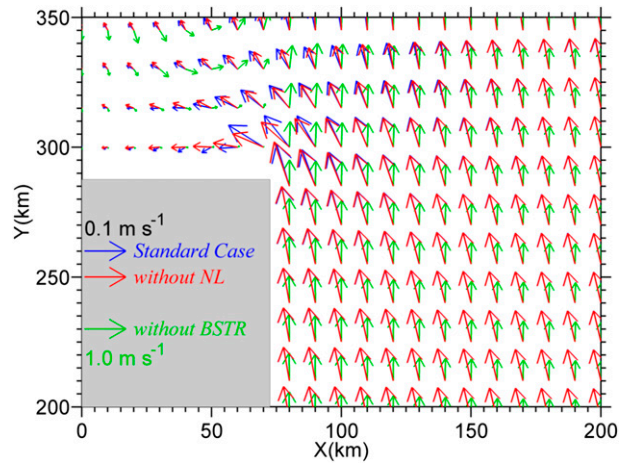


FIG. 14. Bottom velocity vectors (m s^{-1}) for the standard case (blue), as well as for the sensitivity experiments without nonlinear advection term (red) and without bottom stress terms (green) on day 20. NL denotes nonlinear advection, and BSTR represents bottom stress. Note that scale of the vectors is different from the others in the case without BSTR.

The negative bottom shear vorticity is the main contributor to the bottom stress curl. Both negative shear vorticity and positive curvature vorticity at the bottom amplify at the promontory, and the effect of shear vorticity on the bottom stress curl is predominant. Although the shoreward turning of the upwelling jet forms a positive curvature vorticity that weakens the bottom stress curl, it allows the negative vorticity on the seaside of the coastal jet to be situated downstream of the promontory

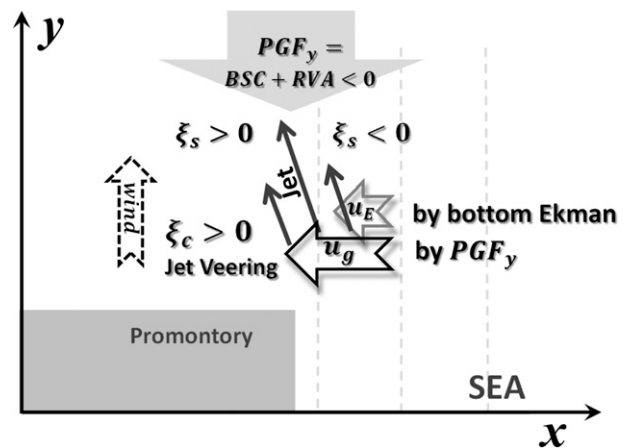


FIG. 15. Schematic showing the intensified cross-shore transport and forcing mechanism in the lee of a coastal promontory. The variables u_E and u_g denote shoreward transport induced by bottom Ekman transport and geostrophic flow due to the negative along-shore PGF_y , respectively; ξ_s is shear vorticity and ξ_c is curvature vorticity.

for local reinforcement of the negative bottom stress curl and thus of negative PGF.

Clearly, the effect of the coastal promontory on the cross-shore transport includes the shoreward veering of the upwelling jet; the formation of the negative shear vorticity at the bottom to create negative bottom stress curl; the formation of the negative vorticity advection in the water column; and, consequently, the formation of a countercurrent PGF for the intensified shoreward transport and upwelling in the lee of the promontory (Fig. 15).

We found that nonlinear advection could change PYB through vorticity advection. However, it also largely alters the bottom stress curl through the bottom shear and curvature vorticity at the same time. These two simultaneous modifications, arising from the nonlinearity of the flow around the promontory, have adverse effect on the PGF and we found that the effect of the nonlinear advection is not significant in changing the characteristics and the intensity of upwelling circulation in the lee of the promontory.

Acknowledgments. This research was supported by the National Key Basic Research Development Program 2009CB421208. We are grateful to the help provided by two anonymous reviewers.

APPENDIX

Bottom Shear and Curvature Vorticity Contributions to the Bottom Stress Curl

The derivation of the contributions of bottom shear (BSC_s) and curvature (BSC_c) vorticity to the total bottom stress curl under the approximation of quadratic drag law [Eq. (5)] is presented in this appendix. According to Gan et al. (2013), the total BSC is expressed as

$$\frac{C_d}{D_{x^*}} \bar{\nabla} \times \frac{\tau_b}{\rho_0} = \frac{C_d}{D_{x^*}} \bar{\nabla} \times \frac{\|\mathbf{V}_b\| \mathbf{V}_b}{\rho_0}, \quad (\text{A1})$$

in which variable $\mathbf{V}_b = (u_b, v_b)$ is the vector form of the bottom velocities in the zonal (u_b) and meridional (v_b) directions. The magnitude of the bottom velocity is represented by $(\mathbf{V}_b) = \sqrt{u_b^2 + v_b^2}$, in which the subscript b denotes the bottom layer. The BSC in Eq. (A1), in Cartesian coordinates, can then be expressed as

$$\begin{aligned} \frac{C_d}{D_{x^*}} \bar{\nabla} \times \frac{\tau_b}{\rho_0} = & \frac{C_d}{D_{x^*}} \left(\|\mathbf{V}_b\| \frac{\partial v_b}{\partial x} - \|\mathbf{V}_b\| \frac{\partial u_b}{\partial y} \right) \\ & + \frac{C_d}{D_{x^*}} \left(v_b \frac{\partial \|\mathbf{V}_b\|}{\partial x} - u_b \frac{\partial \|\mathbf{V}_b\|}{\partial y} \right). \end{aligned} \quad (\text{A2})$$

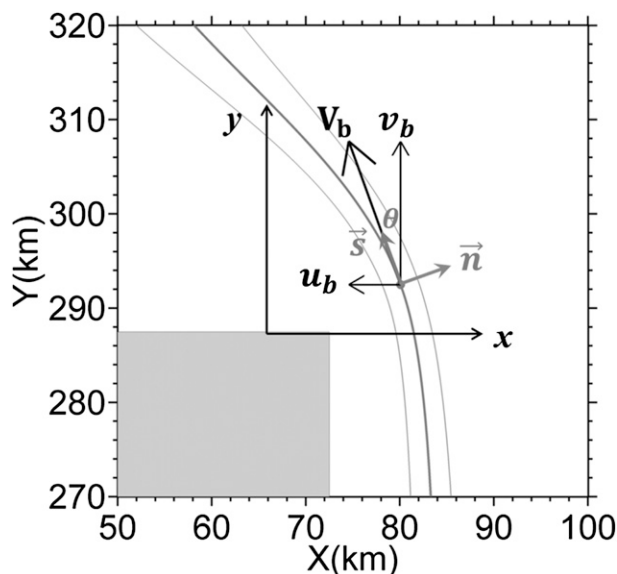


FIG. A1. Sketch of the Cartesian and natural coordinates. The terms \mathbf{n} and \mathbf{s} give the unit vectors in natural coordinates that are perpendicular and parallel to the streamline indicated by the thick gray solid line. The values u_b and v_b are the zonal and meridional bottom velocity components in Cartesian coordinates (x, y), and θ exhibits the transformation angle between the two coordinate systems.

Given the bottom relative vorticity, $\xi_b = (\partial v_b / \partial x) - (\partial u_b / \partial y)$, the first term on the right-hand side of Eq. (A2) is

$$\frac{C_d}{D_{x^*}} \left(\|\mathbf{V}_b\| \frac{\partial v_b}{\partial x} - \|\mathbf{V}_b\| \frac{\partial u_b}{\partial y} \right) = \frac{C_d}{D_{x^*}} \|\mathbf{V}_b\| \xi_b. \quad (\text{A3})$$

For the second term, we adopt a coordinate transformation between the Cartesian and natural coordinates along a streamline bypassing the promontory. The transformation angle between these two coordinate systems is represented by θ , and \mathbf{n} and \mathbf{s} are the unit vectors perpendicular and parallel to the streamline in the natural coordinates (Fig. A1). By definition, the velocity component that is perpendicular to the streamline vanishes, and the bottom relative vorticity ξ_b is the sum of the shear ($\xi_{bs} = \partial \mathbf{V}_b / \partial n$) and curvature ($\xi_{bc} = \mathbf{V}_b / R$) vorticity in the natural coordinates (Holton and Hakim 2004), where R is the radius of curvature of the streamline.

The shear vorticity in the natural coordinates is $\xi_{bs} = \partial \|\mathbf{V}_b\| / \partial n = \mathbf{n} \cdot \nabla \|\mathbf{V}_b\|$, and the unit vector \mathbf{n} can be projected in the Cartesian coordinate system by

$$\mathbf{n} = (n_x, n_y) = (\cos\theta, \sin\theta) = \left(\frac{v_b}{\|\mathbf{V}_b\|}, -\frac{u_b}{\|\mathbf{V}_b\|} \right). \quad (\text{A4})$$

Then, the second term on the right-hand side of Eq. (A2) is

$$\begin{aligned}
& \frac{C_d}{D_{x^*}} \left(v_b \frac{\partial \|\mathbf{V}_b\|}{\partial x} - u_b \frac{\partial \|\mathbf{V}_b\|}{\partial y} \right) \\
&= \frac{C_d}{D_{x^*}} \|\mathbf{V}_b\| \left(\frac{v_b}{\|\mathbf{V}_b\|}, -\frac{u_b}{\|\mathbf{V}_b\|} \right) \cdot \left(\frac{\partial \|\mathbf{V}_b\|}{\partial x}, \frac{\partial \|\mathbf{V}_b\|}{\partial y} \right) \\
&= \frac{C_d}{D_{x^*}} \|\mathbf{V}_b\| (\mathbf{n} \cdot \nabla \|\mathbf{V}_b\|) = \frac{C_d}{D_{x^*}} \|\mathbf{V}_b\| \xi_{bs}.
\end{aligned} \tag{A5}$$

Summing Eqs. (A3) and (A5) and noticing that $\xi_b = \xi_{bs} + \xi_{bc}$, the bottom stress curl in Eq. (A1) is

$$\frac{1}{D_{x^*}} \bar{\mathbf{v}} \times \frac{\boldsymbol{\tau}_b}{\rho_0} = \frac{C_d}{D_{x^*}} \|\mathbf{V}_b\| \xi_{bc} + \frac{2C_d}{D_{x^*}} \|\mathbf{V}_b\| \xi_{bs}, \tag{A6}$$

where the first and second terms in Eq. (A6) represent the contributions from the bottom shear (BSC_s) and curvature (BSC_c) vorticity to the total bottom stress curl, respectively.

REFERENCES

- Allen, J., P. Newberger, and J. Federiuk, 1995: Upwelling circulation on the Oregon continental shelf. Part I: Response to idealized forcing. *J. Phys. Oceanogr.*, **25**, 1843–1866, doi:10.1175/1520-0485(1995)025<1843:UCOTOC>2.0.CO;2.
- Arthur, R. S., 1965: On the calculation of vertical motion in eastern boundary currents from determinations of horizontal motion. *J. Geophys. Res.*, **70** (12), 2799–2803, doi:10.1029/JZ070i012p02799.
- Barth, J. A., S. D. Pierce, and R. L. Smith, 2000: A separating coastal upwelling jet at Cape Blanco, Oregon and its connection to the California Current System. *Deep-Sea Res. II*, **47**, 783–810, doi:10.1016/S0967-0645(99)00127-7.
- Chen, Y. L. L., H. Y. Chen, G. C. Gong, Y. H. Lin, S. Jan, and M. Takahashi, 2004: Phytoplankton production during a summer coastal upwelling in the East China Sea. *Cont. Shelf Res.*, **24**, 1321–1338, doi:10.1016/j.csr.2004.04.002.
- Dale, A. C., and J. A. Barth, 2001: The hydraulics of an evolving upwelling jet flowing around a cape. *J. Phys. Oceanogr.*, **31**, 226–243, doi:10.1175/1520-0485(2001)031<0226:THOAEU>2.0.CO;2.
- Gan, J. P., and J. S. Allen, 2002a: A modeling study of shelf circulation off Northern California in the region of the Coastal Ocean Dynamics Experiment: Response to relaxation of upwelling winds. *J. Geophys. Res.*, **107**, 3123, doi:10.1029/2000JC000768.
- , and —, 2002b: A modeling study of shelf circulation off Northern California in the region of the Coastal Ocean Dynamics Experiment 2. Simulations and comparisons with observations. *J. Geophys. Res.*, **107**, 3184, doi:10.1029/2001JC001190.
- , and —, 2005: On open boundary conditions for a limited-area coastal model off Oregon. Part 1: Response to idealized wind forcing. *Ocean Modell.*, **8**, 115–133, doi:10.1016/j.ocemod.2003.12.006.
- , —, and R. M. Samelson, 2005: On open boundary conditions for a limited-area coastal model off Oregon. Part 2: Response to wind forcing from a regional mesoscale atmospheric model. *Ocean Modell.*, **8**, 155–173, doi:10.1016/j.ocemod.2003.12.007.
- , A. Cheung, X. G. Guo, and L. Li, 2009: Intensified upwelling over a widened shelf in the northeastern South China Sea. *J. Geophys. Res.*, **114**, C09019, doi:10.1029/2007JC004660.
- , H. San Ho, and L. Liang, 2013: Dynamics of intensified downwelling circulation over a widened shelf in the northeastern South China Sea. *J. Phys. Oceanogr.*, **43**, 80–94, doi:10.1175/JPO-D-12-02.1.
- Haidvogel, D. B., A. Beckmann, and K. S. Hedström, 1991: Dynamical simulations of filament formation and evolution in the coastal transition zone. *J. Geophys. Res.*, **96** (C8), 15017–15040, doi:10.1029/91JC00943.
- Holton, J. R., and G. J. Hakim, 2004: *An Introduction to Dynamic Meteorology*. 4th ed. Academic Press, 535 pp.
- Huyer, A., J. H. Fleischbein, J. Keister, P. M. Kosro, N. Perlin, R. L. Smith, and P. A. Wheeler, 2005: Two coastal upwelling domains in the Northern California Current System. *J. Mar. Res.*, **63**, 901–929, doi:10.1357/002224005774464238.
- Janowitz, G. S., and L. J. Pietrafesa, 1982: The effects of alongshore variation in bottom topography on a boundary current—(Topographically induced upwelling). *Cont. Shelf Res.*, **1**, 123–141, doi:10.1016/0278-4343(82)90001-2.
- Kurapov, A. L., J. S. Allen, and G. D. Egbert, 2010: Combined effects of wind-driven upwelling and internal tide on the continental shelf. *J. Phys. Oceanogr.*, **40**, 737–756, doi:10.1175/2009JPO4183.1.
- Liu, X., and J. Su, 1991: Numerical study of coastal upwelling and jet along Zhejiang (in Chinese). *Acta Oceanol. Sin.*, **13**, 305–314.
- Lü, X., F. Qiao, C. Xia, J. Zhu, and Y. Yuan, 2006: Upwelling off Yangtze River estuary in summer. *J. Geophys. Res.*, **111**, C11S08, doi:10.1029/2005JC003250.
- , —, —, and Y. Yuan, 2007: Tidally induced upwelling off Yangtze River estuary and in Zhejiang coastal waters in summer. *Sci. China Ser. D: Earth Sci.*, **50**, 462–473, doi:10.1007/s11430-007-2050-0.
- Marchesiello, P., J. C. McWilliams, and A. Shchepetkin, 2001: Open boundary conditions for long-term integration of regional oceanic models. *Ocean Modell.*, **3**, 1–20, doi:10.1016/S1463-5003(00)00013-5.
- Mellor, G. L., and T. Yamada, 1982: Development of a turbulence closure-model for geophysical fluid problems. *Rev. Geophys.*, **20**, 851–875, doi:10.1029/RG020i004p00851.
- Mertz, G., and D. G. Wright, 1992: Interpretations of JEBAR term. *J. Phys. Oceanogr.*, **22**, 301–305, doi:10.1175/1520-0485(1992)022<0301:IOTJT>2.0.CO;2.
- Pringle, J. M., 2002: Enhancement of wind-driven upwelling and downwelling by alongshore bathymetric variability. *J. Phys. Oceanogr.*, **32**, 3101–3112, doi:10.1175/1520-0485(2002)032<3101:EOWDUA>2.0.CO;2.
- , and E. P. Dever, 2009: Dynamics of wind-driven upwelling and relaxation between Monterey Bay and Point Arena: Local-, regional-, and gyre-scale controls. *J. Geophys. Res.*, **114**, C07003, doi:10.1029/2008JC005016.
- Risien, C. M., and D. B. Chelton, 2008: A global climatology of surface wind and wind stress fields from eight years of QuikSCAT scatterometer data. *J. Phys. Oceanogr.*, **38**, 2379–2413, doi:10.1175/2008JPO3881.1.
- Shchepetkin, A. F., and J. C. McWilliams, 2005: The Regional Oceanic Modeling System (ROMS): A split-explicit, free-surface, topography-following-coordinate oceanic model. *Ocean Modell.*, **9**, 347–404, doi:10.1016/j.ocemod.2004.08.002.
- Song, Y., and D. Haidvogel, 1994: A semi-implicit ocean circulation model using a generalized topography-following

- coordinate system. *J. Comput. Phys.*, **115**, 228–244, doi:10.1006/jcph.1994.1189.
- Song, Y. T., and Y. Chao, 2004: A theoretical study of topographic effects on coastal upwelling and cross-shore exchange. *Ocean Modell.*, **6**, 151–176, doi:10.1016/S1463-5003(02)00064-1.
- , D. B. Haidvogel, and S. M. Glenn, 2001: Effects of topographic variability on the formation of upwelling centers off New Jersey: A theoretical model. *J. Geophys. Res.*, **106** (C5), 9223–9240, doi:10.1029/2000JC000244.
- Tee, K. T., 1985: Depth-dependent studies of tidally induced residual currents on the sides of Georges Bank. *J. Phys. Oceanogr.*, **15**, 1818–1846, doi:10.1175/1520-0485(1985)015<1818:DDSOTI>2.0.CO;2.
- Whitney, M. M., and J. S. Allen, 2009: Coastal wind-driven circulation in the vicinity of a bank. Part I: Modeling flow over idealized symmetric banks. *J. Phys. Oceanogr.*, **39**, 1273–1297, doi:10.1175/2008JPO3966.1.
- Yuan, Y., S. Jilan, and X. Sangyun, 1986: A diagnostic model of summer circulation on the northwest shelf of the East China Sea. *Prog. Oceanogr.*, **17**, 163–176, doi:10.1016/0079-6611(86)90042-X.
- Zhao, B. R., 1993: Upwelling phenomenon off Changjiang estuary. *Acta Oceanol. Sin.*, **15**, 106–114.
- Zhu, J. R., 2003: Dynamic mechanism of the upwelling on the west side of the submerged river valley off the Changjiang mouth in summertime. *Chin. Sci. Bull.*, **48**, 2754–2758, doi:10.1007/BF02901770.